

High-Order Adaptive Extended Stencil FEM with Linear Elements*

Rebecca Conley[†] Tristan J. Delaney[†] Xiangmin Jiao^{†‡}

June 10, 2019

Abstract

The finite element methods are important and powerful tools for solving partial differential equations on complex geometries, but their high-order generalizations pose significant challenges in terms of robustness and mesh generation. In this paper, we introduce a high-order finite element method, which is insensitive to element quality and hence is more robust, and which requires only linear elements even for curved geometries and hence significantly simplifies meshing. Based on our recent work on *Adaptive Extended Stencil FEM*, or *AES-FEM* (*Int. J. Num. Meth. Engrg.*, 2016, DOI:10.1002/nme.5246), the proposed method replaces the traditional interpolatory FEM basis functions with *generalized Lagrange polynomial basis functions*, constructed via local weighted least-squares approximations. In this work, we show that AES-FEM can achieve high-order accuracy using linear elements to discretize the geometry and using the standard FEM hat functions as test functions even for curved geometries. This is in contrast to most high-order generalizations of FEM, which require high-order curved elements for curved geometries. We describe the selection of stencils and the treatment of boundary conditions for high-order AES-FEM, and show that even-degree polynomial basis functions are preferred for even-order PDEs. We present numerical results in 2D and 3D for the Poisson equation and the convection-diffusion equation and demonstrate up to sixth order accuracy with AES-FEM. Overall, AES-FEM is much easier to use than FEM for curved boundaries, while being more accurate, more stable, and more efficient in terms of runtime versus error over relatively fine meshes.

Key Words: finite element methods; partial differential equations; curved boundaries; high-order accuracy; stability; generalized Lagrange polynomial basis

¹This work was partially supported by DoD-ARO under contract #W911NF0910306 and also in part by a subcontract to Stony Brook University from Argonne National Laboratory under Contract DE-AC02-06CH11357 for the SciDAC program funded by the Office of Science, Advanced Scientific Computing Research of the U.S. Department of Energy.

²Dept. of Applied Math. & Stat., Stony Brook University, Stony Brook, NY 11794, USA.

³Corresponding author. Email: xiangmin.jiao@stonybrook.edu.

1 Introduction

Finite element methods (FEM) are one of the most important and powerful tools for solving partial differential equations on complex geometries. FEM originated as a second-order accurate method. For several decades, researchers have been exploring “high-order” variants with third or greater order accuracy. Some high-order methods include isoparametric FEM [14], hp -FEM [12], discontinuous Galerkin methods [10], spectral element methods [8], and isogeometric analysis [18]. Despite the fact that these methods can reach high-order convergence under appropriate conditions, they have remained largely confined to academic research and have yet to make much of an impact in industry [38]. This is due to many reasons, not the least of which are robustness [39] and mesh generation [28]. It is well known that the traditional FEM have a strong dependence on element quality: even just a few “bad” elements can result in ill-conditioned stiffness matrices and hence slow convergence of iterative solvers or loss of accuracy. This problem is even more acute for high-order methods, because most high-order finite element methods require curved elements along boundaries [4], and it difficult to ensure the geometric validity of these elements, especially in 3D [16].

In this paper, we propose a robust, high-order finite element method, which significantly alleviates the requirements on mesh generation. Our approach is based on the *adaptive extended stencil finite element method* or *AES-FEM* (pronounced “ace”-F-E-M) [11]. AES-FEM replaces the piecewise polynomial Lagrange basis functions of the traditional FEM with *generalized Lagrange polynomial (GLP) basis functions*, constructed using local weighted least-squares approximations over adaptively extendable stencils. AES-FEM overcomes the element-quality dependence of the traditional FEM, and allows the use of poorly-shaped elements without compromising accuracy, stability, and efficiency, while preserving the theoretical framework of FEM. The main contribution of the paper is to show that AES-FEM can achieve high-order accuracy using linear elements to discretize the geometry and using the standard FEM hat functions as test functions, even for curved geometries. This is in contrast to most high-order generalizations of FEM, which require high-order curved elements for curved geometries [4, 5, 30]. We present the theoretical analysis of the accuracy of AES-FEM and show that even-degree polynomial basis functions are preferred for even-order PDEs, such as elliptic and parabolic PDEs. We also describe how to select the stencils and how to treat boundary conditions over curved geometries. Our theoretical analyses are further verified via numerical experimentations in 2D and 3D for the Poisson equation and the convection-diffusion equation, which demonstrated up to sixth order accuracy with AES-FEM. Overall, AES-FEM is much easier to use than FEM for curved boundaries, while being more accurate, more stable, and more efficient in terms of runtime versus error over relatively fine meshes. AES-FEM is most applicable to elliptical and parabolic problems. For solving hyperbolic problems, the weighted least squares based essentially non-oscillating (WLS-ENO) scheme has been proposed for finite volume methods in [22], which also uses local weighted least squares

polynomial approximations like AES-FEM.

The remainder of the paper is organized as follows. Section 2 review the background and some related methods, including the basic formulation of AES-FEM. Section 3 addresses some key issues in extending AES-FEM to high-order accuracy, including the selection of stencils and treatment of boundary conditions over curved geometries. Section 4 presents the numerical results to assess its accuracy, stability, and efficiency. Section 5 concludes the paper with a discussion on future work.

2 Background and Related Work

Consider a partial differential equation

$$\mathcal{L}U = \rho \quad (1)$$

on a bounded, simply-connected domain Ω , subject to the Dirichlet and Neumann boundary conditions

$$U = g \text{ on } \Gamma_D \quad \text{and} \quad \frac{\partial U}{\partial \mathbf{n}} = h \text{ on } \Gamma_N. \quad (2)$$

\mathcal{L} denotes a linear differential operator, Γ_D and Γ_N are disjoint sets of the boundary with $\Gamma_D \cup \Gamma_N = \partial\Omega$, and \mathbf{n} denotes the outward normal to Ω . A finite element method, or more generally a weighted-residual method [15], introduces a set of test functions (a.k.a. weight functions) $\Psi = \{\psi_1, \dots, \psi_n\}$, and require the residual $\mathcal{L}U - \rho$ to be orthogonal to Ψ , i.e.,

$$\int_{\Omega} \psi_i (\mathcal{L}U - \rho) \, dV = 0. \quad (3)$$

Eq. (1) and (3) are the *strong form* and *weak form* of the PDE, respectively. In finite element methods, Ψ is typically (weakly) differentiable and has a local support. In addition, Ψ typically forms a partition of unity, i.e., $\sum_{i=1}^n \psi_i = 1$, so that the weighted-residual formulation is global conservative in that $\int_{\Omega} (\mathcal{L}U - \rho) \, dV = 0$.

To find the function U , we further introduce a set of basis functions (a.k.a. trial functions) $\Phi = \{\phi_1, \dots, \phi_n\}$ and define an approximation

$$U \approx \sum_{j=1}^n x_j \phi_j. \quad (4)$$

Substituting (4) into (3) and rearranging the equations, we obtain a system of algebraic equations in x_j ,

$$\sum_{j=1}^n x_j \int_{\Omega} \psi_i (\mathcal{L}\phi_j) \, dV = \int_{\Omega} \psi_i \rho \, dV. \quad (5)$$

If \mathcal{L} involves second or higher order derivatives and the test functions are (weakly) differentiable, integration by parts is often used to reduce the order of the derivatives. When $\Phi = \Psi$, the resulting method is referred to as a Galerkin method; otherwise, it is a Petrov-Galerkin method.

The traditional FEM is a Galerkin method that utilizes piecewise linear polynomial as basis functions. High-order FEM may use a high-degree polynomial basis or a non-polynomial basis, with various choices of test functions. We review some high-order FEM and AES-FEM, on which the method in this paper is based.

2.1 Isoparametric and hp -Adaptive FEM

The isoparametric FEM is a Galerkin method, which uses high-degree Lagrange polynomials as basis functions within each element, defined from equally spaced nodes. These local polynomial basis functions then collectively form C^0 continuous piecewise polynomial basis over Ω [41, 14]. Due to the use of equally spaced nodes, the maximum degree of isoparametric FEM is limited (typically up to six) for stability. If the boundary Γ is curved, isoparametric FEM defines curved elements using the same polynomial basis. The curved elements are necessary for the convergence of isoparametric FEM [4]. At the same time, the curved elements pose significant challenges to mesh generation, because some elements may potentially have negative Jacobian and in turn cause FEM to break down [41]. While significant progress has been made [20, 37], robust generation of high-order meshes has largely remained an open problem, especially in 3D.

The isoparametric FEM in general uses the same-degree polynomial basis uniformly. The p -adaptive FEM generalizes it by allowing the degrees of the basis functions to vary from element to element [35, 2]. The p -adaptivity may be further combined with h -adaptivity, leading to the hp -adaptive FEM or hp -FEM [34, 40]. In these methods, inter-element continuity is typically enforced as constraints [33]. The hp -FEM can achieve high-order convergence, with error decreasing exponentially in the degree of basis functions, provided that the mesh is nearly optimal [12]. Similar to isoparametric FEM, the hp -FEM also requires curved elements for curved geometries, requires good element shapes for accuracy, and is limited to only moderately high orders due to the use of equally spaced nodes.

2.2 Spectral Element Methods and Discontinuous Galerkin

Spectral methods use smooth, global basis functions for solving PDEs [8]. If the solution is smooth, these methods can achieve exponential convergence over simple domains. However, they are not applicable to complex geometries [24]. To handle more general geometries, the spectral element method divides the domain into quadrilateral or hexahedral elements and then uses the concept of spectral methods within each element [26]. Unlike isoparametric elements, the spectral elements tend to use Gaussian quadrature points or Gauss-Lobatto quadrature points as nodes, and hence very high degree polynomials can be

used without instability. Similar to isoparametric elements, spectral elements must also be curved along curved boundaries, and mesh quality is critical for accuracy and stability. Furthermore, generating high-quality quadrilateral and hexahedral meshes is very challenging for complex geometries. Triangle and tetrahedron-based spectral elements have been proposed [36], but it is still an open question regarding the optimal placements of nodes in them [25].

Another class of high-order FEM is the discontinuous Galerkin (DG) methods. Unlike in isoparametric or spectral element methods, the basis functions in DG are not continuous between elements. Instead, a numerical flux is used at the element boundaries. DG is most conveniently applied to hyperbolic PDEs, such as the Navier-Stokes and compressible Euler equations [3, 4], while extensions to parabolic and elliptic problems have also been developed [29]. DG can achieve high-order accuracy and can be used on complex geometries [10], but high-quality curved elements are required for curved boundaries. Other methods related to DG include the interior penalty methods for elliptical problems, which can be unified with DG under one framework [1], the compact DG [27], which has a more compact stencil than local DG methods, and hybridized DG [9], which has a lower number of degrees of freedom.

2.3 Isogeometric Analysis and Meshless Methods

Because the accuracy of geometry is important in FEM, the isogeometric analysis (IGA) was proposed to use exact geometries, represented using NURBS (Non-Uniform Rational B-Splines) or T-splines [18]. Similar to isoparametric elements, IGA uses the same basis functions for both the geometry and solutions. However, unlike isoparametric elements, the basis functions in IGA are C^1 or C^2 continuous, which can be advantages for applications such as thin-shell modeling [18] and can enable more accurate solutions on coarse meshes. However, because the basis functions in IGA are not Lagrange basis, it is more complicated to enforce Dirichlet boundary conditions. In addition, since NURBS and T-splines require well-shaped quadrilaterals and hexahedra, mesh generation for IGA is very challenging. Another related method is the NURBS-enhanced finite element method (NEFEM), which uses NURBS to represent the boundary of the computational domain and uses standard piecewise polynomials for solutions [30]. NEFEM shares the same challenges as IGA in terms of mesh generation.

To overcome mesh dependence, meshless or meshfree methods have been proposed [6, 23]. Like IGA, these methods avoid the use the piecewise polynomials as basis functions. Some meshless methods are Galerkin methods with non-Lagrange basis functions, such as radial basis functions or Shepherd basis functions, which require special quadrature rules and cause complexities in enforcing Dirichlet boundary conditions. Another class of meshless methods is the generalized finite difference (GFD) methods [7], which are weighted residual methods using the Dirac delta functions at the nodes as test functions. When high-degree polynomials are used as basis functions, GFD can achieve high-order accuracy. However, unlike FEM, GFD methods cannot use integration by parts

to reduce the order of derivatives, and are not globally conservative because the test functions do not form a partition of unity.

2.4 Adaptive Extended Stencils FEM (AES-FEM)

The method proposed in this paper is based on AES-FEM [11], which is a Petrov-Galerkin method. Similar to the traditional FEM, AES-FEM uses the standard FEM hat functions as test functions, each of which is associated with an interior node. These test functions are chosen because they are weakly differentiable, have local supports, and form a partition of unity. However, unlike other FEM methods, AES-FEM uses a different set of local basis functions in the neighborhoods of different nodes. Analogous to DG, these locally basis functions do not collectively form C^0 continuous global basis functions. However, unlike in DG, the local basis functions in AES-FEM are constructed node by node instead of element by element.

Consider a node and its associated stencil. Let h be some characteristic length measure of the stencil. The AES-FEM uses the so-called *generalized Lagrange polynomial (GLP)* basis functions defined as follows [11, Definition 1]:

Definition 1. A set of degree- d polynomial basis functions $\{\phi_j\}$ a neighborhood of a point \mathbf{u}_0 constitutes degree- d *GLP basis functions* if $\sum_j \phi_j = 1$ and $\sum_j f(x_j) \phi_j$ approximates a smooth function f to $\mathcal{O}(h^{d+1})$ about \mathbf{u}_0 .

To construct a set of degree- d GLP basis functions, AES-FEM uses a weighted least squares method. Let \mathbf{u} denote the local coordinate system centered at a node \mathbf{u}_0 . Let $\mathcal{P}_k^{(d)}(\mathbf{u})$ denote the set of all k -dimensional monomials of degree d and lower; for example, $\mathcal{P}_2^{(2)}(\mathbf{u}) = [1, u, v, u^2, uv, v^2]^T$. Let $\mathbf{D}_k^{(d)}$ be a diagonal matrix consisting of the fractional factorial part of the coefficients in the Taylor series corresponding to $\mathcal{P}_k^{(d)}$; for example, $\mathbf{D}_2^{(2)} = \text{diag}(1, 1, 1, 1/2, 1, 1/2)$. Then, we may write the truncated Taylor series of a smooth function f as

$$f(\mathbf{u}) \approx \mathbf{c}^T \mathbf{D}_k^{(d)} \mathcal{P}_k^{(d)}(\mathbf{u}). \quad (6)$$

Suppose there are n coefficients in \mathbf{c} . Given the stencil $\{\mathbf{u}_i\}$ about a point \mathbf{u}_0 with m points. To obtain the j th basis function ϕ_j , let $f(\mathbf{u}_i) = \delta_{ij}$. Therefore, we obtain an $m \times n$ least squares problem

$$\mathbf{V} \mathbf{c}_j \approx \mathbf{e}_j, \quad (7)$$

where \mathbf{e}_j denote the j th column of the $m \times m$ identity matrix, and \mathbf{V} is the generalized Vandermonde matrix. Eq. (7) may potentially be ill-conditioned and potentially rank deficient, even if $m \geq n$. We solve (7) by minimizing a weighted norm (or semi-norm)

$$\min_{\mathbf{c}} \|\mathbf{V} \mathbf{c}_j - \mathbf{e}_j\|_{\mathbf{W}} \equiv \min_{\mathbf{c}} \|\mathbf{W}(\mathbf{V} \mathbf{c}_j - \mathbf{e}_j)\|_2, \quad (8)$$

where \mathbf{W} is an $m \times m$ diagonal weighting matrix, and it is a constant for a given node. In general, heavier weights are assigned to nodes that are closer to

\mathbf{u}_0 ; for example,

$$w_i = \left(\frac{\|\mathbf{u}_i\|_2}{h} + \epsilon \right)^{-1}, \quad (9)$$

where ϵ is a small number, such as $\epsilon = 0.01$, for avoiding division by zero.

The matrix \mathbf{WV} can be poorly scaled. We address it by right-multiplying a diagonal matrix \mathbf{S} . Let \mathbf{a}_j denote the j th column of an arbitrary matrix \mathbf{WV} . A typical choice for the i th entry of \mathbf{S} is either $1/\|\mathbf{a}_i\|_2$ or $1/\|\mathbf{a}_i\|_\infty$. After weighting and scaling, the least-squares problem becomes

$$\min_{\mathbf{d}} \left\| \tilde{\mathbf{V}}\mathbf{d} - \mathbf{W}\mathbf{e}_j \right\|_2, \quad \text{where } \tilde{\mathbf{V}} \equiv \mathbf{WVS} \text{ and } \mathbf{d} \equiv \mathbf{S}^{-1}\mathbf{c}_j. \quad (10)$$

Solving the problem using the truncated QR factorization with column pivoting, we have $\mathbf{c}_j = \mathbf{S}\tilde{\mathbf{V}}^+\mathbf{W}\mathbf{e}_j$, where $\tilde{\mathbf{V}}^+$ denote the Moore–Penrose pseudoinverse of $\tilde{\mathbf{V}}$. Thus, the vector \mathbf{c}_j is exactly the j th column of $\mathbf{S}\tilde{\mathbf{V}}^+\mathbf{W}$. A whole set of basis functions is given by

$$\Phi = \left(\mathbf{S}\tilde{\mathbf{V}}^+\mathbf{W} \right)^T \mathbf{D}\mathbf{P}. \quad (11)$$

As shown in Theorem 1 of [11], the set Φ constitutes a set GLP basis functions. This property ensures the consistency of the polynomial approximations in AES-FEM and also eases the strong enforcement of the Dirichlet boundary conditions.

Although the basic formulation of AES-FEM was established in [11], only second-order convergence was demonstrated using quadratic GLP basis. A number of issues remained open for high-order convergence, in terms of the choice of degrees, the selection of stencils, and the treatment of boundary conditions over curved geometries. We address these issues in the next section.

3 High-Order AES-FEM

In this section, we describe the high-order AES-FEM over curved geometries. We will use the Poisson equation as an example, but the idea applies to other PDEs as well.

3.1 Accuracy of AES-FEM

Consider the Poisson equation with Dirichlet boundary conditions, for which (5) becomes

$$\sum_{j=1}^n x_j \int_{\Omega} \psi_i \nabla^2 \phi_j \, dV = \int_{\Omega} \psi_i \rho \, dV. \quad (12)$$

As in FEM, we use integration by parts to reduce the order of derivatives required by (12). If ψ_i has weak derivatives and satisfies the condition $\psi_i|_{\partial\Omega} = 0$,

then after integrating by parts and imposing the boundary conditions, we arrive at

$$-\sum_{j=1}^n x_j \int_{\Omega} \nabla \psi_i \cdot \nabla \phi_j \, dV = \int_{\Omega} \psi_i \rho \, dV. \quad (13)$$

Note that, (13) is often referred to as the weak form of the Poisson equation. Taking (13) over the all the test functions, we obtain a square linear system

$$\mathbf{K}\mathbf{x} = \mathbf{b}, \quad (14)$$

where \mathbf{K} is the stiffness matrix and \mathbf{b} is the load vector, with

$$k_{ij} = - \int_{\Omega} \nabla \psi_i \cdot \nabla \phi_j \, dV \quad \text{and} \quad b_i = \int_{\Omega} \psi_i \rho \, dV. \quad (15)$$

As described in section 2.4, AES-FEM uses the GLP basis functions for ϕ_j . Regardless of the degree of ϕ_j , we use the traditional piecewise-linear FEM shape functions (a.k.a. the hat functions) for ψ_i . The order of convergence of AES-FEM is determined by the degree of the basis functions, as summarized by Theorem 5 in [11].

Theorem 2. *Consider a bounded domain Ω with a piecewise smooth boundary Γ . Suppose U is smooth and thus $\|\nabla U\|$ is bounded. When solving the Poisson equation using AES-FEM with degree- d GLP basis functions in (13), for each ψ_i the weak form (13) is approximated to $\mathcal{O}(ch^d)$, where h is some characteristic length measure of the mesh and $c = \int_{\Omega} \|\nabla \psi_i\| \, dV$.*

Note that in [11], the analysis assumed that $\int_{\Omega} \|\nabla \psi_i\| \, dV = \mathcal{O}(1)$, which holds in 2D but does not hold in other dimensions. For completeness, we include a more general proof in the Appendix. According to the theorem, the truncation error in the weak form is equal to the degree of the GLP basis functions. Analogous to FEM, the AES-FEM is stable if the condition number of the stiffness matrix is $\mathcal{O}(1/h^2)$, independently of element quality. Under the assumption of stability, the global error in U would converge at the same rate as the local truncation errors if there is no systematic cancelation of truncation errors, and the rounding errors do not dominate. This is true for even-degree basis functions for Poisson equations, as we will demonstrate numerically in Section 4.

However, when solving Poisson equations or other elliptic and parabolic PDEs with odd-degree basis functions, the situation is more complicated. In practice, we observe that if the highest-order spatial derivative is even, the order of convergence may be one less than the degree of the basis functions when using odd-degree polynomials. This is because of the cancelation of the odd functions in the integrals over equally spaced grids. To illustrate this effect, let us consider an odd-degree polynomial $f(x) = x^{2m+1}$. Suppose the two elements incident on the node at $x = 0$ are $[-l_1, 0]$ and $[0, l_2]$, and the test function associated the node is ψ . On an equally spaced grid, $l_1 = l_2$, $\psi'(x) = -\psi'(-x)$ and $f'(x) = f'(-x)$. Therefore,

$$\int_{-l}^0 \psi'(x) f'(x) \, dx = - \int_0^l \psi'(x) f'(x) \, dx.$$

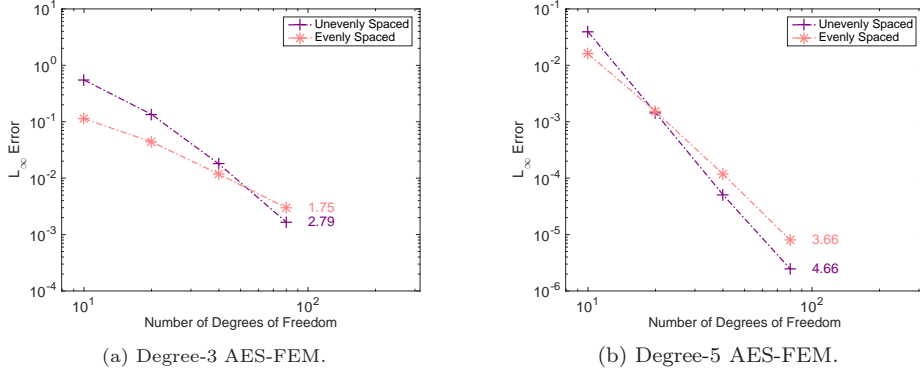


Figure 1: The errors from AES-FEM with odd-degree basis functions for the Poisson equation in 1D. The number to the right of each curve indicates the average convergence rate.

Integrating the weak form corresponding to the test function ψ , we obtain

$$\int_{\Omega} \psi' f' dx = \int_{-l}^l \psi' f' = \int_0^l \psi' f' dx - \int_0^l \psi' f' dx = 0.$$

For nearly even-spaced grids, which is typically the case, the integral corresponding to odd-degree polynomials would be close to zero, so using degree- $(2m + 1)$ polynomials would lead to similar errors as using degree- $2m$ polynomials. Figure 1 demonstrates this behavior numerically with the 1D Poisson equation using degree-3 and 5 basis functions. It can be seen that on highly unequally spaced grids, the convergence rate is approximately equal to the degree of polynomials, but for equally spaced grids, the convergence was lower, although the error may be smaller. We also observe the same behavior in 2D and 3D. Therefore, we should use only even-degree basis functions in the weak forms for even-order PDEs. For odd-order PDEs, odd-degree basis functions are recommended for AES-FEM.

3.2 Selection of Stencils

To achieve high-order accuracy, a critical question is the selection of the stencils at each node for the construction of the GLP basis functions. We utilize meshes for speedy construction of the stencils. Given a simplicial mesh (i.e. a triangle mesh in 2D or a tetrahedral mesh in 3D), the *1-ring neighbor elements* of a node are defined to be the elements incident on the node. The *1-ring neighborhood* of a node contains the nodes of its 1-ring neighbor elements [19]. For any integer $k \geq 1$, we define the *$(k + 1)$ -ring neighborhood* as the nodes in the k -ring neighborhood plus their 1-ring neighborhoods.

The 1-ring neighborhood of a node may supply a sufficient number of nodes for constructing quadratic GLP basis functions. However, 2- and 3-rings are often too large for cubic and quartic constructions. We refine the granularity

Table 1: Comparison of the average number of nodes per ring versus the number of coefficients for 2D (left) and 3D (right) Taylor polynomials.

Degree	#Coeffs.	Ring	#Nodes	Degree	#Coeffs.	Ring	#Nodes
2	6	$1^{1/2}$	12.85	2	10	1	15.46
3	10	2	19.55	3	20	$1^{1/3}$	31.89
4	15	$2^{1/2}$	30.53	4	35	$1^{2/3}$	50.17
5	21	3	39.07	5	56	2	72.64
6	28	$3^{1/2}$	54.80	6	84	$2^{1/3}$	127.83

of the stencils by using fractional rings. In 2D we use half-rings, as defined in [19]. For an integer $k \geq 1$, the $(k + 1/2)$ -ring neighborhood is the k -ring neighborhood together with the nodes of all the faces that share an edge with the k -ring neighborhood. For 3D, we use $1/3$ - and $2/3$ -rings, as defined in [11]. For any integer $k \geq 1$, the $(k + 1/3)$ -ring neighborhood contains the k -ring neighborhood together with the nodes of all elements that share a face with the k -ring neighborhood. The $(k + 2/3)$ -ring neighborhood contains the k -ring neighborhood together with the nodes of all faces that share an edge with the k -ring neighborhood.

In Table 1, we compare the average number of nodes in a given ring, denoted by m , to the number of unknowns for a given degree in (7), denoted by n . We have found that having approximately $m \approx 1.5n$ to $2n$ offers a good balance of accuracy, stability, and efficiency for polynomials up to degree 6. For 2D triangular meshes, the $1^{1/2}$ -ring has an appropriate number of nodes for quadratic basis functions. The 2-ring, $2^{1/2}$ -ring, 3-ring, and $3^{1/2}$ -ring typically provide an appropriate number of nodes for degree 3 to 6 basis functions, respectively. For 3D tetrahedral meshes, the 1-ring, $1^{1/3}$ -ring, $1^{2/3}$ -ring, 2-ring, and $2^{1/3}$ -ring have an appropriate number of nodes for degrees 2 to 6 basis functions, respectively. If a particular neighborhood does not provide enough points, especially for points near boundaries, we further expand the stencil to a larger ring. This allows AES-FEM to overcome element-quality dependence and also to improve the stability of its local computations.

To implement the neighborhood search, we need some an efficient mesh data structure. We use the Array-based Half Facet (AHF) data structure [13], of which the data model is based on the concept of half-facets.

3.3 Treatment of Curved Geometries

Another critical issue of AES-FEM is the resolution of curved geometries. For most high-order FEM methods, elements near the boundary must be curved and approximate the boundary to a high enough order [4, 21]. This is because the mid-edge or mid-face nodes of those high-order elements must approximate the geometry accurately. In AES-FEM, it is also important for all the nodes to approximate the boundary to high-order accuracy. However, because the basis

functions in AES-FEM are constructed from the nodes, independently of the elements, and its test functions are hat functions, AES-FEM uses linear elements without mid-edge or mid-face nodes. Although the linear elements gives only a piecewise linear approximation to the boundary, the effect of this linear approximation is confined in the approximation to the weighted residual formulation (3) without compromising the order of accuracy. Specifically, instead of solving (3), we would be solving a perturbed integral equation

$$\int_{\Omega^h} \psi_i (\mathcal{L}U - \rho) \, dV = 0, \quad (16)$$

where Ω^h denotes the geometric realization of a linear mesh of Ω . Note that (16) remains an exact equality for the exact U and ρ , and hence Theorem (2) remains valid for the equation

$$\int_{\Omega^h} \psi_i \nabla^2 U \, dV = \int_{\Omega^h} \psi_i \rho \, dV \quad (17)$$

in place of (??). Therefore, after substituting the numerical approximations of U into 13, the order of the local truncation errors remains the same, and hence the order of convergence is preserved. The only compromise of using Ω^h instead of Ω is that if the test functions Ψ forms a partition of unity, the global conservation is satisfied in the sense of $\int_{\Omega^h} (\mathcal{L}U - \rho) \, dV = 0$ instead of $\int_{\Omega} (\mathcal{L}U - \rho) \, dV = 0$. This slight deviation of global conservation does not constitute a problem, because global conservation is in general never satisfied exactly even in FEM after boundary conditions are imposed.

To discretize the PDE fully, it is important that boundary conditions are imposed in a fashion that preserves the order of accuracy. For Dirichlet boundary conditions, we enforce them strongly by simply substituting the function values of Dirichlet nodes into the equations, thanks to the use of GLP basis functions. For Neumann boundary conditions, we also propose to impose them strongly by using the Dirac delta function as test functions at Neumann nodes, multiplied by $\mathcal{O}(h^{d-1})$ in d -dimensions to ensure the stiffness matrix is properly scaled. This is analogous to the generalized finite difference method except for the scaling part. This approach ensures the consistency of the discretization, and it avoids the need of high-order accurate boundary integrals, which would have been required if Neumann boundary conditions were to be imposed weakly as in FEM. Note that accurate normals at Neumann nodes are still required, which can be computed to high-order accuracy as described in [19]. In addition, since the stencils for Neumann nodes are one-sided, it requires special care to ensure stability in the computation of the GLP basis functions. We defer the robust treatment of Neumann boundary conditions to future work, and focus on Dirichlet boundary conditions in our numerical experimentations.

4 Numerical Results

In this section, we assess the accuracy, efficiency, and element-quality dependence of AES-FEM with quadratic, quartic, and sextic basis functions, and

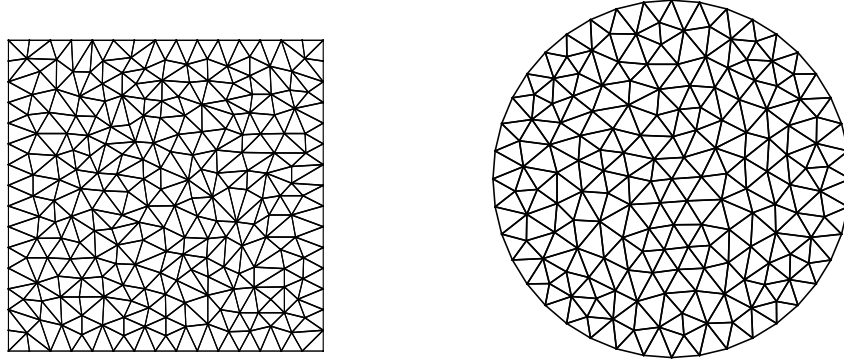


Figure 2: Example 2D meshes with linear elements.

compare it against FEM with linear, quadratic and cubic basis functions. The errors are calculated using the discrete L_2 and L_∞ norms. Let U denote the exact solution and let \tilde{U} denote the numerical solution. Then, we calculate the norms as

$$L_2(\text{error}) = \left(\int_{\Omega} |\tilde{U} - U|^2 \partial\Omega \right)^{1/2} \quad \text{and} \quad L_\infty(\text{error}) = \max_i |\tilde{U} - U|. \quad (18)$$

On a series of meshes of different grid resolution, we calculate the average convergence rate as

$$\text{convergence rate} = -\log_2 \left(\frac{\text{error on } m_c}{\text{error on } m_f} \right) \Big/ \log_2 \left(\sqrt[d]{\frac{\text{nodes in } m_c}{\text{nodes in } m_f}} \right), \quad (19)$$

where d is the spacial dimension, m_c is the coarsest mesh, and m_f is the finest mesh.

4.1 2D Results

We first assess AES-FEM in 2D over the unit square and the unit disc, which are representative for geometries with flat and curved boundaries, respectively. We triangulated the domains using Triangle [31] for linear meshes and using Gmsh [17] for quadratic and cubic meshes. See Figure 2 for some examples meshes with linear elements, which are representative in terms of mesh quality but are coarser than those used in actual computations. The numbers of nodes for the unit square range from 1,027 to 146,077, and those for the unit disc range from 544 to 79,417. Since isoparametric FEM requires good mesh quality, we ensured that these meshes all have good element shapes for our comparative study: For linear meshes, the minimum angle is 24.04 degrees and the maximum angle is 128.17 degrees; for high-order meshes, all elements have positive Jacobians everywhere.

We consider the Poisson equation and convention-diffusion equation. For both cases, we use GMRES with the ILU preconditioner to solve the linear systems arising from AES-FEM. For FEM, we use conjugate gradient (CG) with incomplete Cholesky as the preconditioner for the Poisson equation, and use GMRES with ILU for the convection-diffusion equation. To demonstrate the accuracy of high-order methods, we set the tolerance of the iterative solvers to 10^{-12} . The drop tolerance for the incomplete factorization is set as 10^{-4} by default, unless otherwise noted.

4.1.1 Poisson Equation

We first present results for the Poisson equation with Dirichlet boundary conditions on the unit square and on the unit disc. That is,

$$-\nabla^2 U = \rho \quad \text{in } \Omega, \quad (20)$$

$$U = g \quad \text{on } \partial\Omega. \quad (21)$$

For the unit square $\Omega = [0, 1]^2$, we consider the following three analytic solutions:

$$U_1 = 16x^3(1-x^3)y^3(1-y^3), \quad (22)$$

$$U_2 = \cos(\pi x) \cos(\pi y), \quad (23)$$

$$U_3 = \frac{\sinh(\pi x) \cosh(\pi y)}{\sinh \pi \cosh \pi}. \quad (24)$$

For the unit disc $\Omega = \{(x, y) | x^2 + y^2 \leq 1\}$, we consider U_3 and also

$$U_4 = \cos\left(\frac{\pi}{2}(x^2 + y^2)\right).$$

For each problem, the right-hand side ρ and the Dirichlet boundary condition g are obtained from the given analytic solutions. For all the cases, the iterative solvers converged to the desired tolerance for AES-FEM. For FEM, the solver stagnated for the finest meshes in some cases without achieving the specified tolerance, even after we reduced the drop tolerance to 10^{-6} in incomplete Cholesky. However, the resulting errors were small enough not to affect the comparison qualitatively.

Figure 3 shows the L_∞ and L_2 norm errors for U_1 on the unit square. The L_2 norm errors for U_2 and U_3 on the unit square and for U_3 and U_4 on the unit disc are shown in Figures 4 and 5, respectively. In all cases, quadratic AES-FEM and linear FEM have similar errors, and quartic AES-FEM has similar or better results compared to cubic FEM. Both of the above pairs have similar sparsity patterns and similar numbers of nonzeros in the coefficient matrices. Furthermore, sextic AES-FEM is far more accurate than all the other methods, achieving sixth-order accuracy despite the use of linear elements. This result confirms our accuracy analysis in Section 3 for 2D problems.

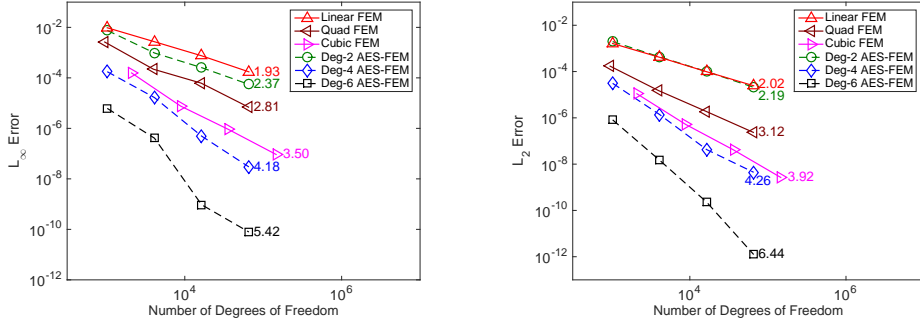


Figure 3: The errors for 2D Poisson equation on the unit square for U_1 in L_∞ (left) and L_2 norms (right). The number to the right of each curve indicates the average convergence rate.

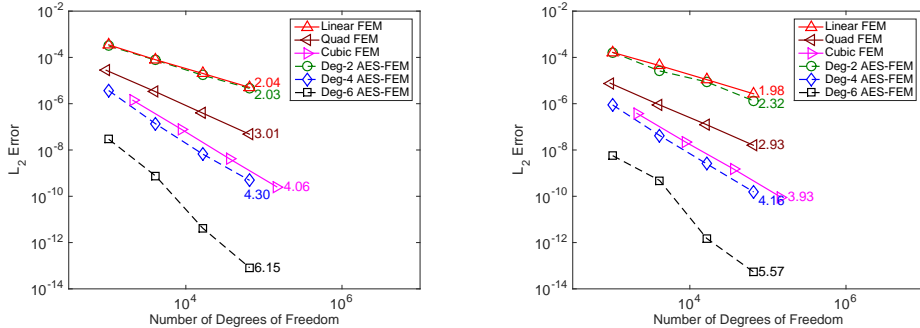


Figure 4: The L_2 norm errors for 2D Poisson equation on the unit square for U_2 (left) and U_3 (right).

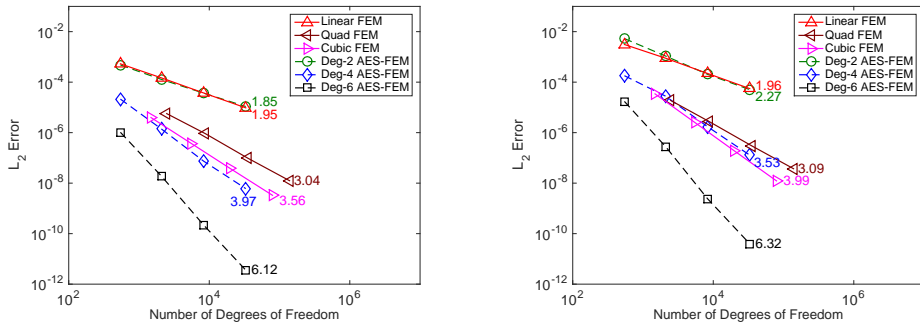


Figure 5: The L_2 norm errors for 2D Poisson equation on the unit disc for U_3 (left) and U_4 (right).

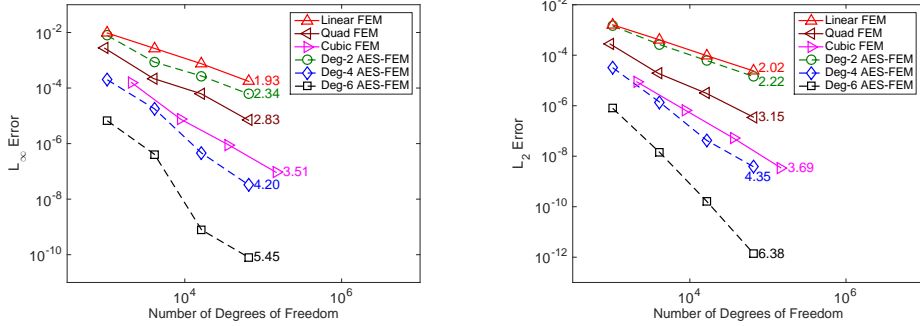


Figure 6: The errors for 2D convection-diffusion equation on the unit square for U_1 in the infinity norm (left) and the L_2 norm (right).

4.1.2 Convection-Diffusion Equation

In our second example, we consider the time-independent convection-diffusion equation with Dirichlet boundary conditions, that is,

$$-\nabla^2 U + \mathbf{c} \cdot \nabla U = \rho \quad \text{in } \Omega, \quad (25)$$

$$U = g \quad \text{on } \partial\Omega. \quad (26)$$

We take $\mathbf{c} = [1, 1]^T$ for all of our tests, and we consider the same analytic solutions over the unit square and on the unit disc as for the Poisson equation.

Figure 6 shows the L_∞ and L_2 norm errors for U_1 on the unit square. The L_2 norm errors for U_2 and U_3 on the unit square and for U_3 and U_4 on the unit disc are shown in Figures 7 and 8, respectively. Similar to the Poisson equation, quadratic AES-FEM has similar convergence rate as linear FEM, but slightly lower errors. Quartic AES-FEM is more accurate than cubic FEM in all cases, and sextic AES-FEM again delivers superior accuracy, achieving about sixth-order convergence.

4.1.3 Assessment of Element-Quality Dependence

To assess the dependence of AES-FEM and FEM on mesh quality, we use a series of meshes for the unit square with progressively worse element quality, which we obtain by distorting a good-quality mesh. For AES-FEM and linear FEM, we use a mesh with 130,288 elements and 65,655 nodes and distort four elements by moving one vertex of each of these elements incrementally towards its opposite edge. For quadratic FEM, we use a mesh with 32,292 elements and 65,093 nodes and distort a single element by moving one vertex its adjacent mid-edge nodes incrementally towards its opposite edge. For cubic FEM, we use a mesh with 32,292 elements and 146,077 nodes, and distort a single element by

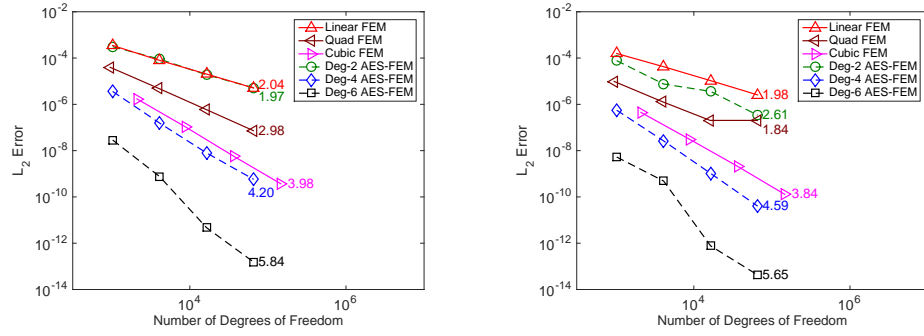


Figure 7: The L_2 norm errors for 2D convection-diffusion equation on the unit square for U_2 (left) and U_3 (right).

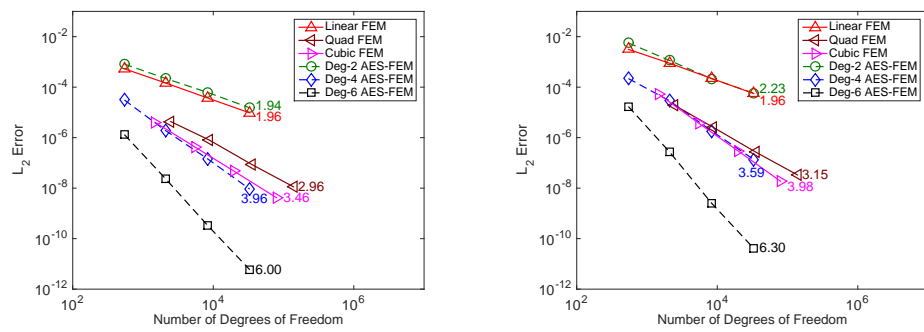


Figure 8: The L_2 norm errors for 2D convection-diffusion equation on the unit disc for U_3 (left) and U_4 (right).

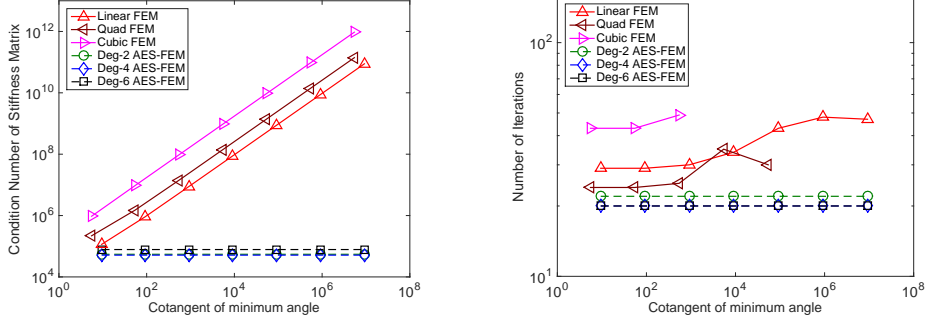


Figure 9: Left: the lower bound of the condition numbers of the stiffness matrices of FEM and AES-FEM method on a series of progressive worse meshes in 2D. Right: the number of iterations required for the iterative solver to converge when solving the corresponding systems.

moving one vertex and its adjacent mid-edge nodes. On each distorted mesh, we solve the Poisson equation with the exact solution U_2 .

Figure 9 shows the condition numbers of the stiffness matrices of FEM and AES-FEM and the numbers of iterations required to solve the linear systems. It can be seen that the condition numbers of FEM increase inversely proportional to the minimum angle, while the condition numbers of AES-FEM remain constant. In terms of the linear solver, the numbers of iteration increase significantly for linear FEM as the mesh is distorted, and preconditioned CG fails for poorly-shaped quadratic and cubic meshes due to nonpositive pivot during incomplete Cholesky or due to stagnation of CG. In contrast, the number of iterations remains constant for AES-FEM, independently of the element quality.

4.1.4 Efficiency

To compare the efficiency of AES-FEM and FEM, Figures 10 and 11 show the errors versus runtimes for the 2D Poisson equation and convection-diffusion equation, respectively. It is evident that for the convection-diffusion equation, both quartic and sextic AES-FEM outperform cubic FEM over relatively fine meshes. For the Poisson equation, sextic AES-FEM outperforms cubic FEM over finer meshes on the unit square, and on the unit disc, both quartic and sextic outperform cubic FEM. We expect AES-FEM will perform even better with further optimization of its implementation.

4.2 3D Results

We now assess AES-FEM in 3D over the unit cube and the unit ball, which are representative for geometries with flat and curved boundaries, respectively. We mesh the domains using TenGen [32] for the linear meshes and using Gmsh for

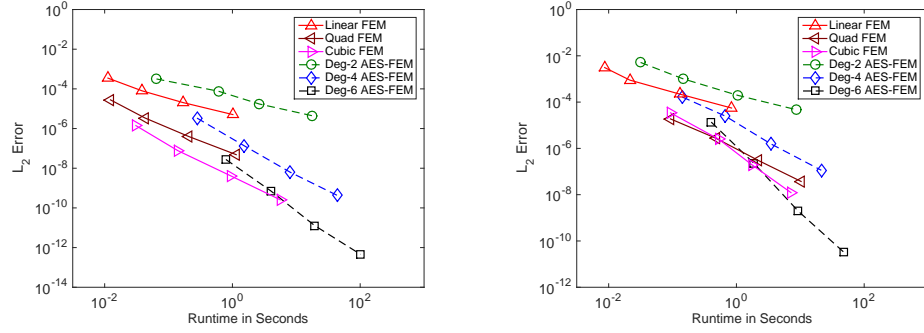


Figure 10: The errors verses runtime for 2D Poisson equation on the unit square for exact solution U_2 (left) and on the unit disc for exact solution U_4 (right).

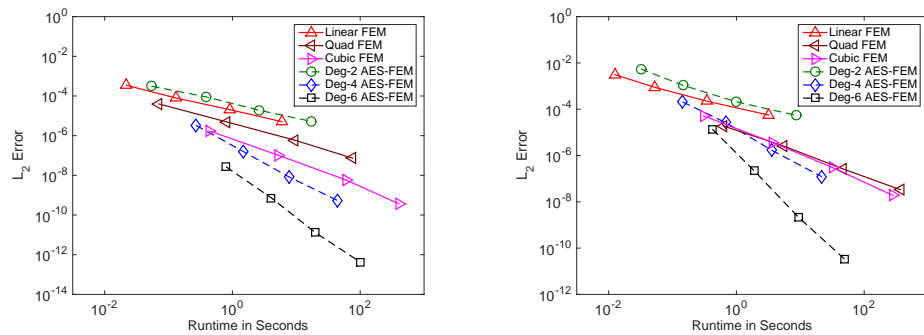


Figure 11: The errors verses runtime for 2D convection-diffusion equation on the unit square for exact solution U_2 (left) and on the unit disc for exact solution U_4 (right).

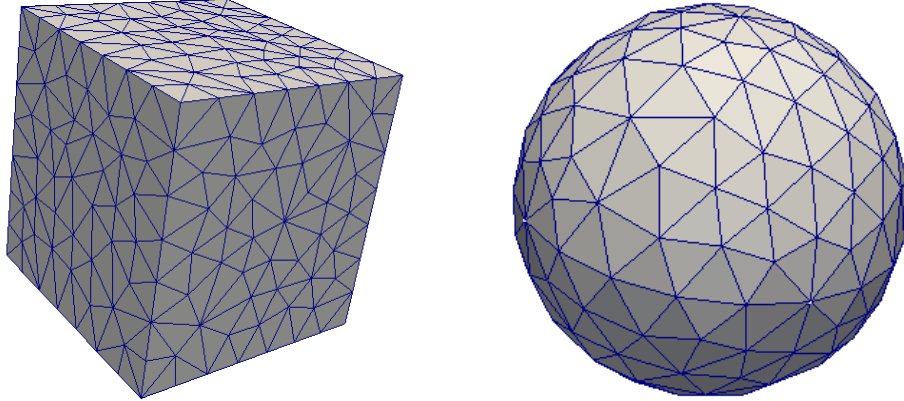


Figure 12: Example 3D meshes with linear elements.

the quadratic and cubic meshes. See Figure 12 for some example meshes with linear elements, which are representative in terms of mesh quality but are coarser than those used in actual computations. The numbers of nodes for the unit cube range from 509 to 7,272,811, and those for the unit ball range from 1,011 to 2,834,229. As in 2D, since isoparametric FEM requires good mesh quality, we ensured that these meshes all have reasonable element shapes: For linear meshes, the minimum dihedral angle is 6.09 degrees and the maximum angle is 166.05 degrees; for high-order meshes, all elements have positive Jacobians everywhere.

We consider the Poisson equation and the convection-diffusion equation. For both cases, we use GMRES with the Gauss-Seidel preconditioner to solve the linear systems arising from AES-FEM. For FEM, we use CG with incomplete Cholesky as the preconditioner for the Poisson equation, and use GMRES with Gauss-Seidel for the convection-diffusion equation. We set the tolerance of the iterative solvers to 10^{-12} . The drop tolerance for incomplete Cholesky is 10^{-3} on the cube and 10^{-6} on the ball.

4.2.1 Poisson Equation

We first present results for the Poisson equation with Dirichlet boundary conditions on the unit cube and on the unit ball. That is,

$$-\nabla^2 U = \rho \quad \text{in } \Omega, \tag{27}$$

$$U = g \quad \text{on } \partial\Omega. \tag{28}$$

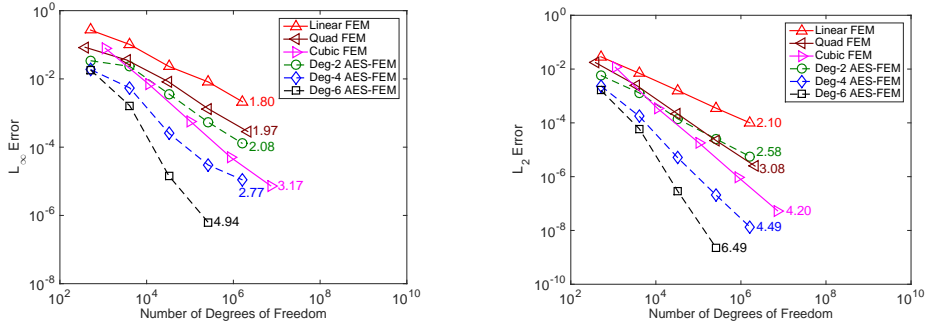


Figure 13: The errors for 3D Poisson equation on the unit cube for U_1 in the infinity norm (left) and L_2 norm (right).

For the unit cube, where $\Omega = [0, 1]^3$, we consider the following three analytic solutions:

$$U_1 = 64x^3(1 - x^3)y^3(1 - y^3)z^3(1 - z^3), \quad (29)$$

$$U_2 = \cos(\pi x)\cos(\pi y)\cos(\pi z), \quad (30)$$

$$U_3 = \frac{\sinh(\pi x)\cosh(\pi y)\cosh(\pi z)}{\sinh \pi \cosh^2 \pi}. \quad (31)$$

For the unit ball $\Omega = \{(x, y, z) | x^2 + y^2 + z^2 \leq 1\}$, we consider the analytic solution U_4 and also

$$U_4 = \cos\left(\frac{\pi}{2}(x^2 + y^2 + z^2)\right).$$

For each problem, the right-hand side ρ and the Dirichlet boundary conditions g are obtained from the given analytic solutions.

Figure 13 shows the L_∞ and L_2 norm errors for U_1 on the unit cube. The L_2 norm errors for U_2 and U_3 on the unit cube and for U_3 and U_4 on the unit ball are in Figures 14 and 15, respectively. In all cases, quadratic AES-FEM converges at similar or better rates than linear FEM and has lower errors, and quartic AES-FEM has similar or lower errors than cubic FEM. As in 2D, both of the aforementioned pairs have similar sparsity patterns and similar numbers of nonzeros in the coefficient matrices. Furthermore, sextic AES-FEM is far more accurate than all the other meshes, achieving sixth-order accuracy despite the use of linear elements. This further confirms our accuracy analysis in Section 3 for 3D problems.

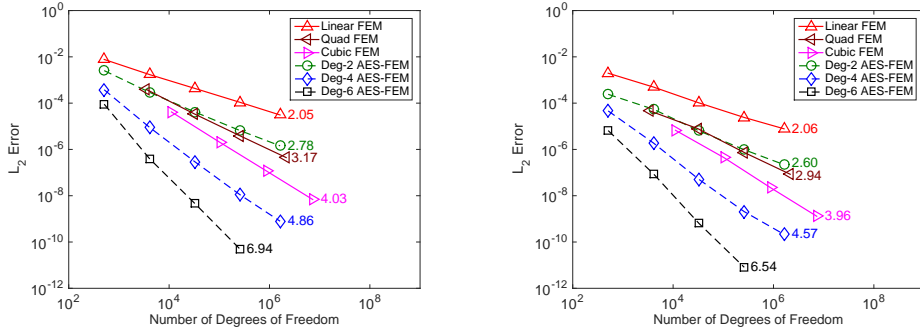


Figure 14: The L_2 norm errors for 3D Poisson equation on the unit cube for U_2 (left) and U_3 (right).

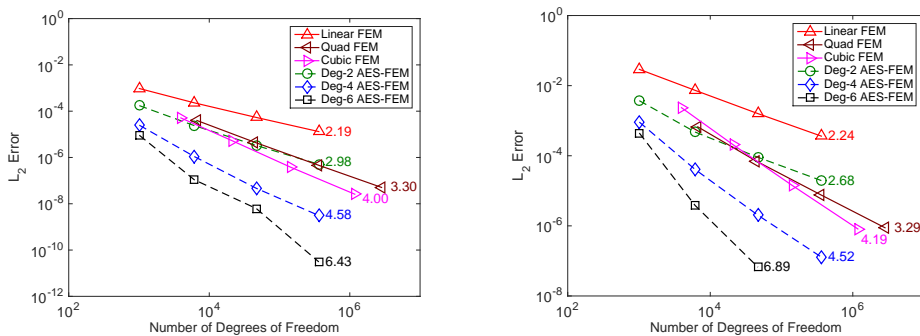


Figure 15: The L_2 norm errors for 3D Poisson equation on the unit ball for U_3 (left) and U_4 (right).

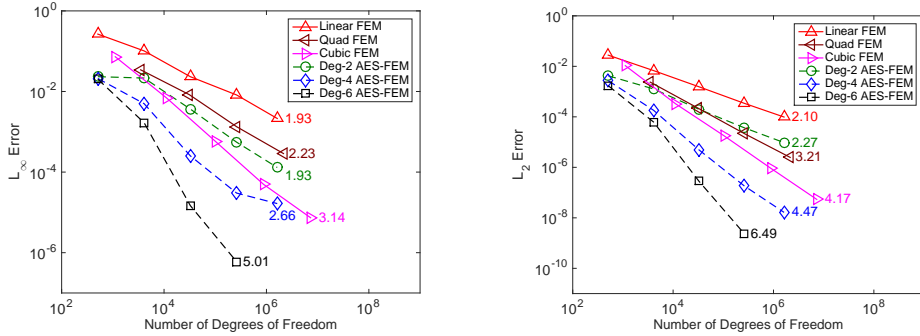


Figure 16: The errors for 3D convection-diffusion equation on the unit cube for U_1 in the infinity norm (left) and L_2 norm (right).

4.2.2 Convection-Diffusion Equation

We consider the time-independent convection-diffusion equation with Dirichlet boundary conditions on the unit cube and the unit ball, that is,

$$-\nabla^2 U + \mathbf{c} \cdot \nabla U = \rho \quad \text{in } \Omega, \quad (32)$$

$$U = g \quad \text{on } \partial\Omega. \quad (33)$$

We take $\mathbf{c} = [1, 1, 1]^T$ and we consider the same analytic solutions over the unit cube and unit ball as for the Poisson equation.

Figure 16 shows the L_∞ and L_2 norm errors for U_1 on the unit cube. The L_2 norm errors for U_2 and U_3 on the unit cube and for U_3 and U_4 on the unit ball are in Figures 17 and 18, respectively. Similar to the Poisson equation, quadratic AES-FEM and linear FEM converge at similar rates with quadratic AES-FEM having slightly lower errors. Quartic AES-FEM is more accurate than the cubic FEM in all cases, and sextic AES-FEM is again the most accurate, with about sixth-order convergence. For FEM, the linear solver stagnated for the same problems on the finest mesh, but the resulting errors were small enough not to affect the comparison qualitatively.

4.2.3 Assessment of Element-Quality Dependence

To assess the dependence of AES-FEM and FEM on mesh quality in 3D, we use a series of meshes on the unit cube with progressively worse element quality, which we obtain by distorting a good-quality mesh. For AES-FEM and linear FEM, we use a mesh with 1,500,282 elements and 262,144 nodes and distort 74 elements by moving one vertex of each of these elements incrementally towards its opposite face. For quadratic FEM, we use a mesh with 178,746 elements and 250,047 nodes and distort nine elements by moving one vertex of each of

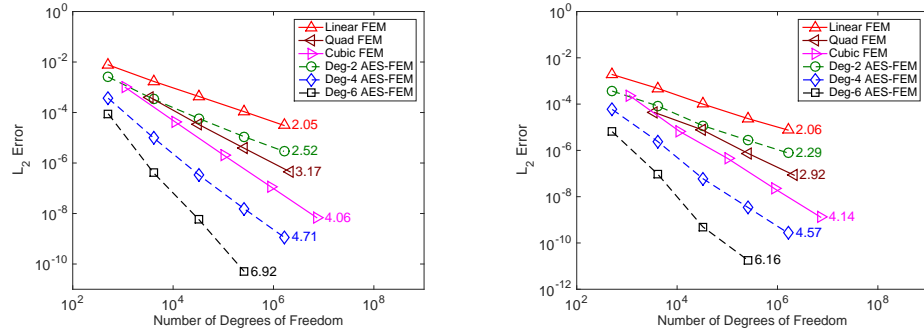


Figure 17: The L_2 norm errors for 3D convection-diffusion equation on the unit cube for U_2 (left) and U_3 (right).

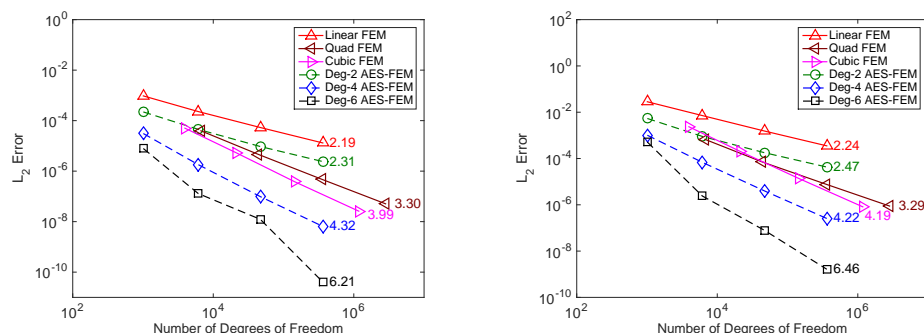


Figure 18: The L_2 norm errors for 3D convection-diffusion equation on the unit ball for U_3 (left) and U_4 (right).

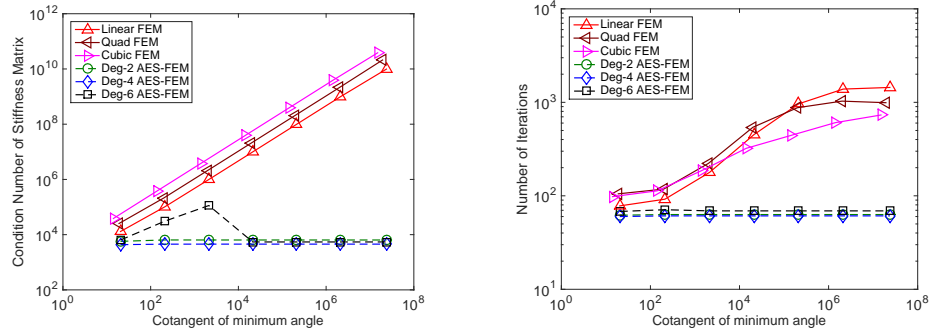


Figure 19: Left: the estimated condition numbers of the stiffness matrices of FEM and AES-FEM method on a series of progressive worse meshes in 3D. Right: the number of iterations required for the iterative solver to converge when solving the corresponding systems.

these elements and their adjacent mid-edge and mid-face nodes incrementally towards its opposite face. For cubic FEM, a mesh with 20,250 elements and 97,336 nodes is used and distort a single element by moving one vertex and its adjacent mid-edge, mid-face, and mid-cell nodes incrementally towards its opposite face.

On each distorted mesh, we solve the Poisson equation with the exact solution U_2 . The iterative solvers used are GMRES for AES-FEM and CG for FEM. The tolerance for both solvers is 10^{-8} . The preconditioner used for both methods is Gauss-Seidel.

Figure 19 shows the condition numbers of the stiffness matrices of FEM and AES-FEM and the numbers of iterations required to solve the linear systems. It can be seen that the condition numbers of FEM increase inversely proportional to the minimum angle, while the condition numbers of quadratic and quartic AES-FEM remain constant. The condition numbers of sextic AES-FEM increase slightly for the second and third meshes, but then dropped back to the original number. In terms of the linear solver, the number of iterations increases significantly for FEM while remaining constant for AES-FEM, independent of element quality.

4.2.4 Efficiency

To compare the efficiency of AES-FEM and FEM in 3D, Figures 20 and 21 show the errors versus runtimes for the 3D Poisson equation and convection-diffusion equation, respectively. It is evident that on relatively finer meshes, sextic AES-FEM outperforms cubic FEM, and for the Poisson equation on the unit ball, quartic AES-FEM does as well. We expect AES-FEM will perform even better with further code optimizations.

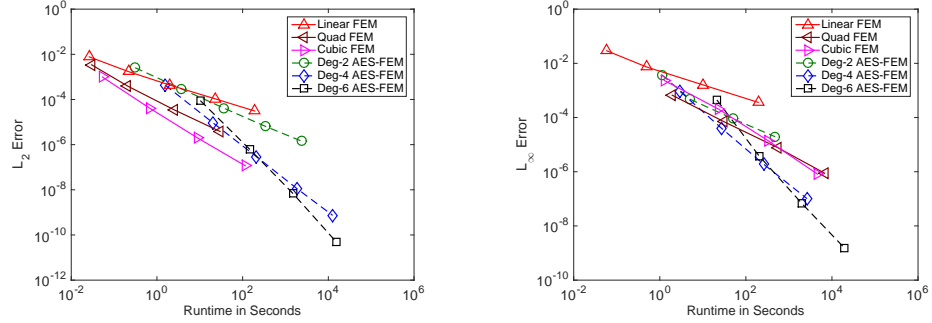


Figure 20: The errors verses runtime for 3D Poisson equation on the unit cube for exact solution U_2 (left) and on the unit ball for exact solution U_4 (right).

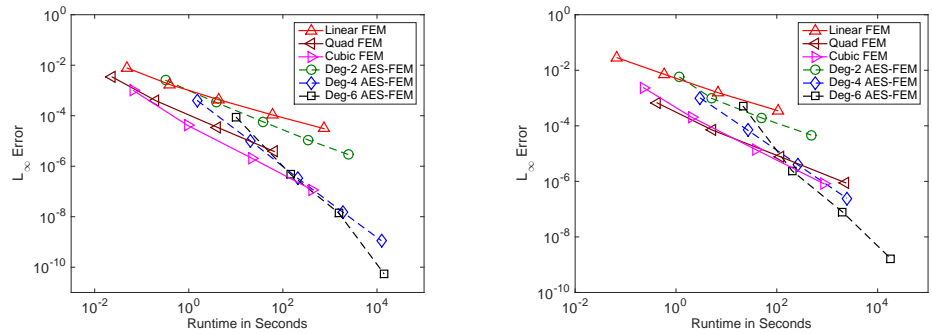


Figure 21: The errors verses runtime for 3D convection-diffusion equation on the unit cube for exact solution U_2 (left) and on the unit ball for exact solution U_4 (right).

5 Conclusions

In this paper, we presented an extension of AES-FEM, which achieves high-order accuracy using only linear elements even for curved geometries. As the original AES-FEM, the high-order variant uses the generalized Lagrange polynomial (GLP) basis functions constructed using weighted least squares over an extended stencil at each node, while using piecewise linear hat-functions as test functions. This choice allows AES-FEM to overcome the dependence of element quality, and to simplify mesh generation for curved geometries, both of which have been significant challenges for the traditional FEM. We rigorously analyzed the order of convergence of high-order AES-FEM and showed that even-degree polynomials are in general preferred for solving even-order PDEs, such as elliptic and parabolic problems. For different degrees of basis functions, we presented guidelines for selecting stencils over simplicial meshes in 2-D and 3-D. We also described how to enforce essential and natural boundary conditions strongly, so that using linear elements would not compromise the order of convergence. We compared the accuracy of quadratic, quartic and sextic AES-FEM against linear, quadratic and cubic FEM in 2-D and 3-D, including on domains with curved boundaries. We demonstrated improved accuracy and stability of high-order AES-FEM over high-order FEM and demonstrated up to sixth-order convergence rates of AES-FEM despite the use of linear elements. We showed that the condition number of the stiffness matrix resulting from high-order AES-FEM, and hence the number of iterations required to solve the system, are independent of the element quality. Our results also showed that quartic and sextic AES-FEM are more efficient cubic FEM on fine meshes in terms of error versus runtime for Poisson and convection-diffusion equations. Future work includes further optimization of performance by exploring p -adaptivity and efficient parallel implementations and multigrid solvers, and further enhancement of robustness over tangled meshes and one-sided stencils.

Acknowledgements

Results were obtained using the high-performance LI-RED computing system at the Institute for Advanced Computational Science at Stony Brook University, which was obtained through the Empire State Development grant NYS #28451.

References

- [1] D. N. ARNOLD, F. BREZZI, B. COCKBURN, AND L. D. MARINI, *Unified analysis of discontinuous Galerkin methods for elliptic problems*, SIAM J. Numer. Anal., 39 (2002), pp. 1749–1779.
- [2] I. BABUSKA, B. A. SZABO, AND I. N. KATZ, *The p -version of the finite element method*, SIAM J. Numer. Anal., 18 (1981), pp. 515–545.

- [3] F. BASSI AND S. REBAY, *A high-order accurate discontinuous finite element method for the numerical solution of the compressible Navier–Stokes equations*, J. Comput. Phys., 131 (1997), pp. 267–279.
- [4] F. BASSI AND S. REBAY, *High-order accurate discontinuous finite element solution of the 2D Euler equations*, J. Comput. Phys., 138 (1997), pp. 251–285.
- [5] Y. BAZILEVS, V. M. CALO, J. A. COTTRELL, J. A. EVANS, T. HUGHES, S. LIPTON, M. SCOTT, AND T. SEDERBERG, *Isogeometric analysis using T-splines*, Comput. Meth. Appl. Mech. Engrg., 199 (2010), pp. 229–263.
- [6] T. BELYTSCHKO, Y. KRONGAUZ, D. ORGAN, M. FLEMING, AND P. KRYSL, *Meshless methods: An overview and recent developments*, Comput. Methods Appl. Mech. Engrg., 139 (1996), pp. 3–47.
- [7] J. BENITO, F. UREÑA, AND L. GAVETE, *Solving parabolic and hyperbolic equations by the generalized finite difference method*, J. Comput. Appl. Math., 209 (2007), pp. 208–233.
- [8] C. CANUTO, M. Y. HUSSAINI, A. M. QUARTERONI, A. THOMAS JR, ET AL., *Spectral methods in fluid dynamics*, Springer Science & Business Media, Berlin Heidelberg, 2012.
- [9] B. COCKBURN, J. GOPALAKRISHNAN, AND R. LAZAROV, *Unified hybridization of discontinuous Galerkin, mixed, and continuous Galerkin methods for second order elliptic problems*, SIAM J. Numer. Anal., 47 (2009), pp. 1319–1365.
- [10] B. COCKBURN, G. E. KARNIADAKIS, AND C.-W. SHU, *The Development of Discontinuous Galerkin Methods*, Springer, 2000.
- [11] R. CONLEY, T. J. DELANEY, AND X. JIAO, *Overcoming element quality dependence of finite elements with adaptive extended stencil FEM (AES-FEM)*, Int. J. Numer. Meth. Engng., (2016). doi:10.1002/nme.5246.
- [12] L. DEMKOWICZ, W. RACHOWICZ, AND P. DEVLOO, *A fully automatic hp-adaptivity*, SIAM J. Sci. Comput., 17 (2002), pp. 117–142.
- [13] V. DYEDOV, N. RAY, D. EINSTEIN, X. JIAO, AND T. J. TAUTGES, *AHF: Array-based half-facet data structure for mixed-dimensional and non-manifold meshes*, in Proceedings of the 22nd International Meshing Roundtable, Springer, Orlando, Florida, 2014, pp. 445–464.
- [14] I. ERGATOUDIS, B. IRONS, AND O. ZIENKIEWICZ, *Curved, isoparametric, “quadrilateral” elements for finite element analysis*, Int. J. Solids Struct., 4 (1968), pp. 31–42.
- [15] B. A. FINLAYSON, *The Method of Weighted Residuals and Variational Principles*, Academic Press, New York, 1973.

- [16] A. GARGALLO-PEIRÓ, X. ROCA, J. PERAIRE, AND J. SARRATE, *Defining quality measures for validation and generation of high-order tetrahedral meshes*, in Proceedings of the 22nd International Meshing Roundtable, Springer, 2014, pp. 109–126.
- [17] C. GEUZAIN AND J.-F. REMACLE, *Gmsh: A 3-d finite element mesh generator with built-in pre-and post-processing facilities*, Int. J. Numer. Meth. Engrg., 79 (2009), pp. 1309–1331.
- [18] T. J. HUGHES, J. A. COTTRELL, AND Y. BAZILEVS, *Isogeometric analysis: CAD, finite elements, NURBS, exact geometry and mesh refinement*, Comput. Meth. Appl. Mech. Engrg., 194 (2005), pp. 4135–4195.
- [19] X. JIAO AND H. ZHA, *Consistent computation of first-and second-order differential quantities for surface meshes*, in ACM Symposium on Solid and Physical Modeling, ACM, 2008, pp. 159–170.
- [20] A. JOHNEN, J.-F. REMACLE, AND C. GEUZAIN, *Geometrical validity of curvilinear finite elements*, J. Comput. Phys., 233 (2013), pp. 359–372.
- [21] M. LENOIR, *Optimal isoparametric finite elements and error estimates for domains involving curved boundaries*, SIAM J. Numer. Anal., 23 (1986), pp. 562–580.
- [22] H. LIU AND X. JIAO, *WLS-ENO: Weighted least squares based essentially non-oscillatory schemes on unstructured meshes*, J. Comput. Phys., (2016) (In press)). DOI: 10.1016/j.jcp.2016.03.039.
- [23] J. T. ODEN, C. A. M. DUARTE, AND O. C. ZIENKIEWICZ, *A new cloud-based hp finite element method*, Comput. Methods Appl. Mech. Engrg., 153 (1998), pp. 117–126.
- [24] R. PASQUETTI AND F. RAPETTI, *Spectral element methods on triangles and quadrilaterals: comparisons and applications*, J. Comput. Phys., 198 (2004), pp. 349–362.
- [25] ———, *Spectral element methods on unstructured meshes: which interpolation points?*, Numer. Algorithms, 55 (2010), pp. 349–366.
- [26] A. T. PATERA, *A spectral element method for fluid dynamics: Laminar flow in a channel expansion*, J. Comput. Phys., 54 (1984), pp. 468–488.
- [27] J. PERAIRE AND P.-O. PERSSON, *The compact discontinuous Galerkin (CDG) method for elliptic problems*, SIAM J. Sci. Comput., 30 (2008), pp. 1806–1824.
- [28] P.-O. PERSSON AND J. PERAIRE, *Curved mesh generation and mesh refinement using Lagrangian solid mechanics*, in Proceedings of the 47th AIAA Aerospace Sciences Meeting and Exhibit, vol. 204, 2009.

- [29] B. RIVIÈRE, *Discontinuous Galerkin methods for solving elliptic and parabolic equations: theory and implementation*, SIAM, 2008.
- [30] R. SEVILLA, S. FERNÁNDEZ-MÉNDEZ, AND A. HUERTA, *NURBS-enhanced finite element method (NEFEM)*, Int. J. Numer. Meth. Engng., 76 (2008), pp. 56–83.
- [31] J. R. SHEWCHUK, *Triangle: Engineering a 2D quality mesh generator and Delaunay triangulator*, in Applied Computational Geometry Towards Geometric Engineering, Springer, 1996, pp. 203–222.
- [32] H. SI, *TetGen, a Delaunay-based quality tetrahedral mesh generator*, ACM Trans. Math. Software, 41 (2015), pp. 11:1 – 11:36.
- [33] P. ŠOLÍN, J. ČERVENÝ, AND I. DOLEŽEL, *Arbitrary-level hanging nodes and automatic adaptivity in the hp-FEM*, Math. Comput. Simulat., 77 (2008), pp. 117–132.
- [34] P. ŠOLÍN, K. SEGETH, AND I. DOLEŽEL, *Higher-order finite element methods*, CRC Press, 2003.
- [35] B. SZABO AND A. MEHTA, *p -convergent finite element approximations in fracture mechanics*, Int. J. Numer. Meth. Engng., 12 (1978), pp. 551–560.
- [36] M. A. TAYLOR AND B. WINGATE, *A generalized diagonal mass matrix spectral element method for non-quadrilateral elements*, Appl. Numer. Math., 33 (2000), pp. 259–265.
- [37] T. TOULORGE, C. GEUZAIN, J.-F. REMACLE, AND J. LAMBRECHTS, *Robust untangling of curvilinear meshes*, J. Comput. Phys., 254 (2013), pp. 8–26.
- [38] P. VINCENT AND A. JAMESON, *Facilitating the adoption of unstructured high-order methods amongst a wider community of fluid dynamicists*, Math. Model. Nat. Phenom., 6 (2011), pp. 97–140.
- [39] Z. WANG, *High-order methods for the Euler and Navier–Stokes equations on unstructured grids*, Prog. Aerosp. Sc., 43 (2007), pp. 1–41.
- [40] N. ZANDER, T. BOG, S. KOLLMANSBERGER, D. SCHILLINGER, AND E. RANK, *Multi-level hp-adaptivity: high-order mesh adaptivity without the difficulties of constraining hanging nodes*, Comput. Mech., 55 (2015), pp. 499–517.
- [41] O. ZIENKIEWICZ, R. TAYLOR, AND J. ZHU, *The Finite Element Method: Its Basis and Fundamentals*, Butterworth-Heinemann, Oxford, 7th ed., 2013.

Appendix: Proof of Theorem 2

Let U be the exact solution on a mesh with mesh size h , and let

$$\tilde{U} = \sum_{j=1}^n U_i \phi_j$$

denote the approximation to U using degree- d GLP basis functions. When using degree- d GLP basis functions, it follows from Lemma 3 in [11] that

$$\|\nabla U - \nabla \tilde{U}\| = \mathcal{O}(h^d)$$

within each element. Under the assumption that U is twice differentiable, ∇U is bounded, and hence

$$\left| \int_{\Omega} (\nabla U - \nabla \tilde{U}) \cdot \nabla \psi_i \, dV \right| = \mathcal{O}(h^d) \left| \int_{\Omega} \nabla U \cdot \nabla \psi_i \, dV \right|.$$

Assume $\|\nabla U\|$ is bounded, then $\left| \int_{\Omega} \nabla U \cdot \nabla \psi_i \, dV \right| = \mathcal{O}(\int_{\Omega} \|\nabla \psi_i\| \, dV)$.

Furthermore, if ρ is approximated by degree- d GLP basis functions as $\tilde{\rho} = \sum_{j=1}^n \rho_i \phi_j$, then we have $\left| \int_{\Omega} (\rho - \tilde{\rho}) \psi_i \, dV \right| = \mathcal{O}(h^{d+1}) \left| \int_{\Omega} \rho \psi_i \, dV \right|$. Assume ρ is bounded, then $\left| \int_{\Omega} \rho \psi_i \, dV \right| = \mathcal{O}(\int_{\Omega} \psi_i \, dV)$, which is higher order than $\int_{\Omega} \|\nabla \psi_i\| \, dV$ for hat functions. Therefore, the residual in the weak form is $\mathcal{O}(ch^d)$, where $c = \mathcal{O}(\int_{\Omega} \|\nabla \psi_i\| \, dV)$.